Available online at www.sciencedirect.com
SCIENCE DIRECT®
Surface and Coatings Technology 172 (2003) 24–41
SURFACE & COATINGS TECHNOLOGY
www.elsevier.com/locate/surfcoat

The effects of fuel chemistry and feedstock powder structure on the mechanical and tribological properties of HVOF thermal-sprayed WC–Co coatings with very fine structures

Yunfei Qiao[a,1], Traugott E. Fischer[a,*], Andrew Dent[b]

[a]*Department of Chemical, Biochemical and Materials Engineering, Stevens Institute of Technology, Hoboken, NJ 07030, USA*
[b]*Center for Thermal Spray Research (CTSR), SUNY at Stony Brook, Stony Brook, NY 11794-2275, USA*

Received 26 April 2002; accepted in revised form 20 January 2003

Abstract

We have deposited a series of WC–Co coatings by the high velocity oxy fuel (HVOF) process, using three different powders, and different spray conditions. The powders are a nanocrystalline (Nanocarb), a near-nanostructured powder (Infralloy) containing a proprietary additive aimed at retarding grain growth, and multimodal (mixed micro and nano) powder (Nanomyte). HVOF spray conditions were stoichiometric, fuel rich and oxygen rich. 'In-flight' feedstock powder temperature and velocity were measured. The hardness and toughness of the coatings are found to depend on WC-binder adhesion and adhesion between splats. High flame temperatures increase WC-binder adhesion but increase decarburization. The latter is found to decrease adhesion between the splats. Decarburization is most pronounced for nanostructured powders because of their high specific surface. The additive in Infralloy decreases adhesion between WC grains and binder, but it also reduces decarburization. The wear resistance of the coatings increases with hardness and decreases with increasing decarburization. Sliding wear occurs by a attrition of the WC grains and the lifting of entire splats; abrasive wear occurs by ductile cutting, grain loss and lifting of splats; the low wear rate in sliding leads to splat-boundary weakening by fatigue. The effect of decarburization predominates in sliding wear and is less pronounced in abrasion; the high abrasive wear removes material before fatigue becomes important. The coating deposited at high temperature, from the multimodal powder Nanomyte, presents outstanding sliding and abrasive wear resistance but inflicts large wear on the opposing silicon nitride surface in sliding. Coatings deposited with the near nanostructured powder containing an additive present high sliding wear resistance, independent of the deposition parameters, and cause low wear of the opposing silicon nitride. Coatings deposited with spray-dried nanostructured powders offer comparatively low wear resistance, in agreement with previous reports.

Keywords: WC–Co; Nanostructure; Decarburization; Microstructure; Nanoporosity; Hardness; Toughness; Sliding wear; Abrasive wear

1. Introduction

The reduction of WC grain size, to the nanometer range, [1] has resulted in increased hardness [2] and resistance to abrasive [3] and sliding wear [4] of sintered, bulk, WC–Co composites. It is therefore worth exploring whether similar improvements in performance can be obtained in thermal-sprayed WC–Co coatings [5–8]. It is well known, however, that the thermal spray process introduces a number of specific flaws that limit the performance of the coatings [9–12]. For thermal spraying, the WC–Co material is agglomerated into particles, usually in the range of 30–50 μm, that are injected into the flame of the spray gun where they are partially molten and accelerated to high velocities toward the substrate. The morphology and porosity of the particles and the flame characteristics determine the temperature and velocity of the particles in the jet, and thereby the amount of decarburization, the porosity, and the cohesion of the coating.

Usmani and Sampath [5] and Stewart et al. [6] have reported disappointing sliding wear and abrasive wear resistance of nanostructured WC–Co coatings deposited

*Corresponding author. Tel.: +1-201-216-5266; fax: +1-201-216-8306.
E-mail address: tfischer@stevens-tech.edu (T.E. Fischer).
[1] Present address: SuperPower, Inc. 450 Duane Avenue, Schenectady, NY 12304, USA.

0257-8972/03/$ - see front matter © 2003 Elsevier Science B.V. All rights reserved.
doi:10.1016/S0257-8972(03)00242-1

Table 1
Chemistry and deposition conditions of WC–Co coatings

Sample	Powder	Co (%)	Part. size (μm)	Carbide size (μm)	Spray condition	Fuel–Oxygen ratio	Porosity (%)[a]	WC (%)	W_2C (%)	W (%)	Amorphous phase (%)
NC8N	Nanocarb®	15	41	0.03–0.05	Neutral	0.23	1.7	67.5	14.5	13	5
NC8O	Nanocarb®	15	41	0.03–0.05	Oxidizing	0.17	2.9	70.5	19	8	2.5
NC8R	Nanocarb®	15	41	0.03–0.05	Reducing	0.29	2.9	89.2	9.3	0	1.5
IN8N	Infralloy®	12	24	0.2–0.3	Neutral	0.23	1.9	87	13	0	0
IN8O	Infralloy®	12	24	0.2–0.3	Oxidizing	0.17	2.1	99.5	0.5	0	0
IN8R	Infralloy®	12	24	0.2–0.3	Reducing	0.29	2.1	98.5	1	0	0.5
NM8N	Nanomyte®	12	26	0.03–3	Neutral	0.23	1.6	80	11.2	8.8	0
NM8O	Nanomyte®	12	26	0.03–3	Oxidizing	0.17	2.4	86.3	8.7	5	0
NM8R	Nanomyte®	12	26	0.03–3	Reducing	0.29	2.0	97.6	1.4	1	0
DM8N	Diamalloy®	12	25	2–3	Neutral	0.23	1.8	72.4	27.6		

[a] This is macroporosity according to ASTM standard.

with powders that were prepared with the spray-dry process [1]. These authors have identified increased decarburization of the coatings as the origin of their disappointing performance. In fact, Stewart et al. [6] have shown that the large surface-to-volume ratio of commercially available nanostructured WC powders increases their tendency toward decarburization. Our previous investigation of a large number of coatings [7] has provided a quantitative overview of the influences of spray process and powder properties on the tribological performance of the thermal sprayed WC–Co coatings. It has largely confirmed the findings of Refs. [5,6]; it has also shown that sliding and abrasive wear resistances do not respond identically to material properties. It is evident that the achievement of superior wear resistance from nanostructured coatings would require an optimization of the powder preparation and a readaptation of the spay process.

In the present investigation, we explored novel coatings deposited with three different WC–Co powders with very fine WC grains and with different settings of the spray torch that produced different flame temperatures and chemistries. A detailed examination of their microstructure will provide us with further insight into the spray process and the way it determines the mechanical properties of the coatings. We describe the hardness, toughness, the sliding and abrasive wear behavior of these coatings. We will relate the tribological performance of the coatings to their microstructure, as it is determined by the parameters of the spray process and the structure of the feedstock powders.

2. Deposition of the coatings

2.1. The feedstock powders

Three different powders were used as feedstock in the present investigation. These were nanocrystalline WC–15Co Nanocarb® (NC) provided by Union Minière (former Nanodyne Inc.), New Brunswick, NJ; ultrafine WC–12Co Infralloy® (IN) provided by Inframat Corporation, North Haven, CT and multimodal WC–12Co Nanomyte® (NM) provided by Nanopowder Enterprises Inc., Piscataway, NJ. The characteristics of the powders are given in Table 1, and scanning electron microscope (SEM) images of the powders are shown in Fig. 1. The particle size distributions of the feedstock powders have been measured by a Microtrac SRA system. In the following, 'grain' will denote WC grain and 'particle' will denote agglomerate.

The Nanocarb® powder presents a typical spray-drying morphology in which the carbide and cobalt are combined together in 30–50 nm grains due to chemical reaction as shown in Fig. 1a; the small grains are porous and present a relatively large surface to volume ratio. The Nanocarb® agglomerate particles are hollow spheres (Fig. 1a); their size is in the range of 5–90 μm with an average of 41 μm.

The Infralloy® powder is doped with a small amount of a proprietary additive to retard grain growth; it was agglomerated in a proprietary process aiming at high density. This powder is composed of densely packed 200–300 nm carbides that show an acicular morphology revealing their crystal structure (Fig. 1b). The size of Infralloy® powders is distributed in the range of 5–60 μm with an average of 24 μm.

The Nanomyte® powder [8] is composed of 70% coarse (2–3 μm) and 30% (30–50 nm) nanocrystalline carbides as shown in Fig. 1c. The nanocrystalline carbides are evenly distributed between the coarse carbides. The Nanomyte® powder was agglomerated by sintering; the particle size distribution is 5–60 μm with an average of 26 μm.

For comparison, a commercial Diamalloy® WC–12Co powder produced by Sulzer Metco was sprayed with the same gun in neutral flame. The Diamalloy® powder is composed of 2–3 μm carbides with an average particle size of approximately 25 μm as shown in Fig. 1d.

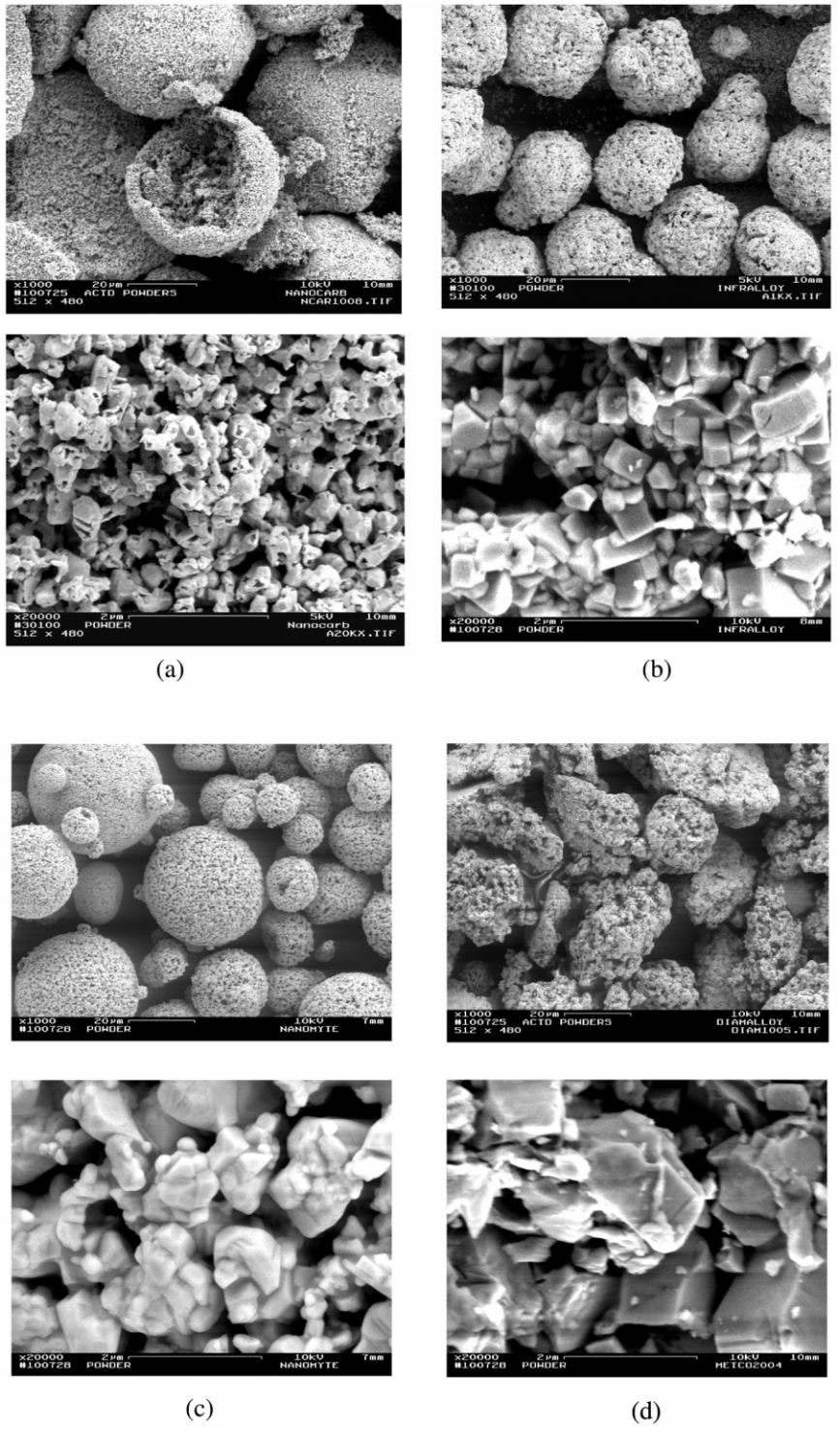

Fig. 1. Morphology of WC–15Co Nanocarb® powders. (a-1) The agglomerated particles; (a-2) high resolution view of the surface of an agglomerate. (b) Morphology of WC–12Co Infralloy® powders. (b-1) The agglomerated particles; (b-2) high resolution view of the surface of an agglomerate. (c) Morphology of WC–12Co Nanomyte® powders. (c-1) The agglomerated particles; (c-2) high resolution view of the surface of an agglomerate. (d) Morphology of WC–12Co Diamalloy® commercial powders. (d-1) The agglomerated particles; (d-2) high resolution view of the surface of an agglomerate.

2.2. Deposition techniques

The coatings were sprayed at CTSR, SUNY, Stony Brook, NY using a Sulzer Metco DJ2700 hybrid diamond jet. This gun is equipped with an elongated, water-cooled, nozzle that permits higher gas temperatures (3000 °C), and higher gas pressures than conventional guns. Therefore, it can produce higher particle temperatures and velocities than the standard DJ spray gun. Propylene was chosen as the fuel gas. The spray distance was 0.2 m (8 inches) from the nozzle exit. Three spray chemistries; neutral (N), reducing (R) and oxidizing (O), were used. The neutral condition corresponds to the optimum combustion in which the fuel–oxygen ratio is stoichiometric and the flame enthalpy is maximum. Reducing condition was fuel rich and oxidizing was oxygen rich. The stoichiometric fuel–oxygen ratio is $2/9=0.222$. Since 20% oxygen is present in the high-pressure air used to transport the feedstock powders, the fuel–oxygen ratio of the neutral flame was chosen as 0.23, as listed in Table 1. The fuel–oxygen ratio of the reducing and oxidizing flames was set at 0.29 and 0.17 as listed in Table 1. The powder used, the spray distance, in inches (8), and the flame chemistry designate the samples.

In-flight temperature and velocity of the powders were measured using a Technar DPV 2000 system. In the neutral condition all three feedstock powders have achieved the highest temperature, approximately 2200 °C, and the highest velocity, approximately 700 m/s. Since the combustion in the reducing and oxidizing flame is not complete, powder temperatures (1550–1800 °C) and velocities (450–550 m/s) are lower than in the neutral flame. These velocities and temperatures are shown in Fig. 2 in relation to the hardness of the coatings obtained.

2.3. Decarburization of the coatings

During the deposition, the material loses a certain amount of its carbon [9–13]. In order to determine the amount of decarburization, we analyzed the phase constituents in the coatings using a Siemens D5000 X-ray diffractometer with Cu Kα ($\lambda=0.15406$ nm) radiation at 40 kV and 30 mA. A low scanning rate of 0.1°/min was used to achieve the desired precision. The amount of decarburization, calculated from the integrated intensities of diffraction peaks, is listed in Table 1. All three types of coatings suffer the highest decarburization when sprayed in the neutral flame because of its high temperature. Coatings sprayed in the oxidizing flame suffer higher decarburization than those sprayed in the reducing flame (at roughly similar temperatures), except samples IN8O and IN8R. These samples, with their additive to retard grain growth, appear more sensitive to temperature than to chemistry.

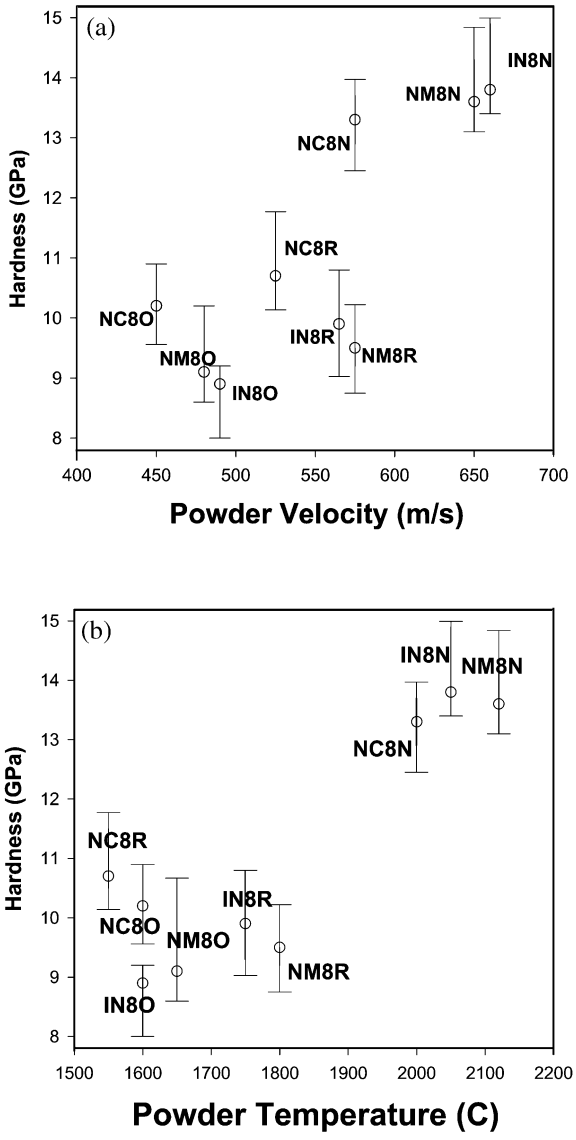

Fig. 2. (a) Coating hardness at 300 g indentation load as a function of 'in-flight' powder velocity. (b) Coating hardness at 300 g indentation load as a function of 'in-flight' powder temperature.

Our X-ray diffraction (XRD) patterns are similar to others published before and will not be shown. They contain WC, W_2C and W peaks and a broad shoulder at the place of the cobalt peaks, showing that the binder is in amorphous or nanocrystalline form [12,13].

Nanocarb® suffers the most decarburization in all three flames due to its high surface to volume ratio, which enables it to react faster with the flame, despite its larger agglomerate size and lower temperature. In the neutral and oxidizing flames, the Nanocarb® coatings contain tungsten in addition to WC and W_2C. We shall return to this point later in examining the microstructures of the coatings.

Infralloy® powder has the highest decarburization resistance in all three flames due to the additive and a

denser agglomerate. The additives have the effect of preventing diffusion of tungsten and carbon into the cobalt matrix. Its low decarburization is especially pronounced in the neutral and oxidizing flame, as listed in Table 1. Interestingly, the XRD patterns of samples IN8O and IN8R, which are not decarburized, show no trace of cobalt, either crystalline or amorphous. It appears that the carbon-poor cobalt in these samples is susceptible to evaporation or oxidation by the flame. In contrast, decarburization in the other powders occurs through dissolution of W and C in the cobalt, which is protected by preferential oxidation of carbon.

3. Mechanical properties

3.1. Hardness

The hardness of the coatings was measured with a Vickers indenter on the surfaces and cross-sections previously polished to a final roughness R_a 0.03–0.04 μm with 30, 6 and 1 μm grade diamond in three sequential steps. The hardness on the surface was measured with loads varying from 0.05 to 50 kg. The hardness on the cross-section was measured at 300 and 1000 g load. The distance between indentations was large enough to avoid interaction between the work-hardened regions and any micro-cracks caused by the indentations. The coatings were thick enough (300–500 μm) to ensure valid hardness measurement on the surface. Six indentations were made at each load. The hardness of thermally sprayed WC–Co coatings varies considerably over each sample surface; these variations have been shown to correlate with variations in sliding wear resistance [14]. The hardness and its variations are shown in Fig. 2. The average of the six measurements is reported in Table 1. The hardness of the WC–Co is primarily determined by the powder velocity and temperature as shown in Fig. 4a and b. We note that the hardness/temperature ratio of the Nanocarb® samples, (NC8O and NC8R), especially at low temperature, is higher than for the other samples. We shall see later that this is attributable to the more thorough melting allowed by their high surface areas.

The dependence of hardness on indentation load is shown in Fig. 3. Such dependence is common in all materials, but the one shown in the figure is larger than that of sintered WC–Co [2]. In the low load range, the hardness varies by 20% for the coatings sprayed in the neutral flame, and 30% for those sprayed with reducing and oxidizing flames. Over the entire load range of 50 g to 20 kg, the hardness varies by 30% for the harder coatings, i.e. those sprayed in the neutral flame, and 40% for the softer ones, i.e. those sprayed with reducing and oxidizing flames. We shall discuss the hardness of the samples below, in light of their microstructures.

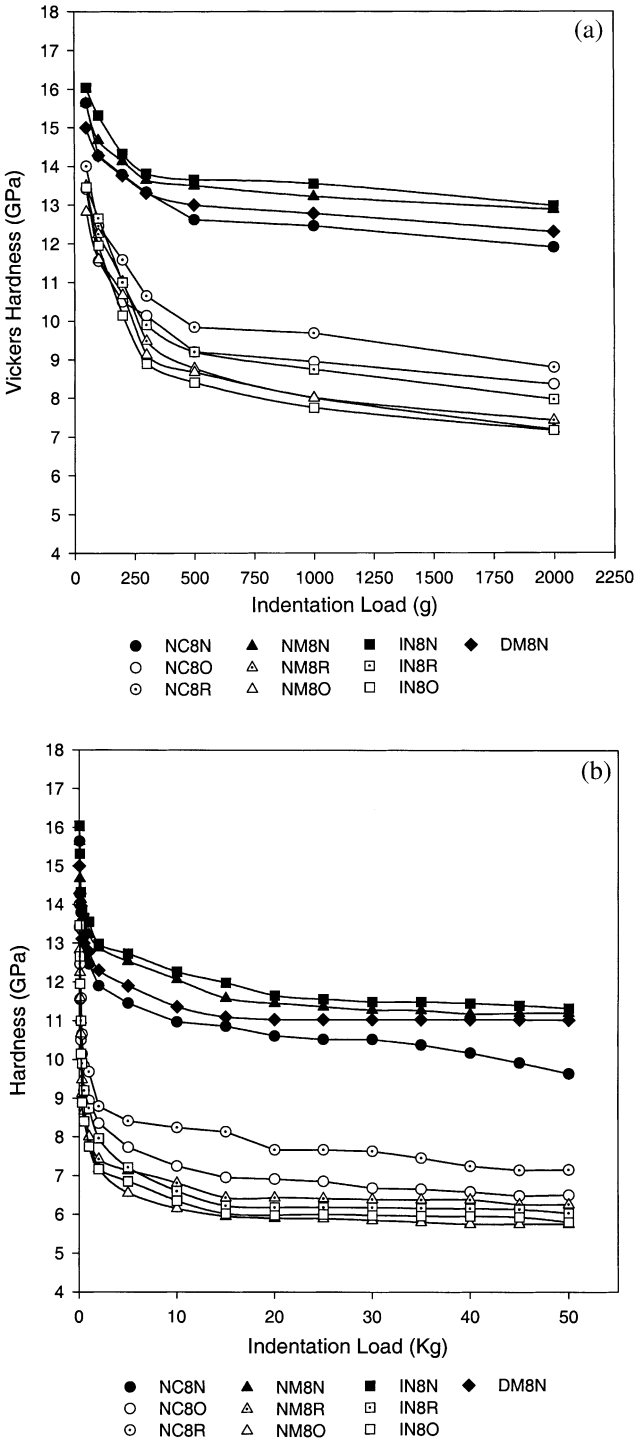

Fig. 3. (a) Coating hardness as a function of load in the of range 50 gf to 2 kgf. (b) Indentation hardness as a function of load in the range 50 gf to 50 kgf.

3.2. Fracture toughness

The toughness of coatings is most conveniently measured from the radial (Palmqvist) cracks emanating from the corners of indentations at high loads. A number of

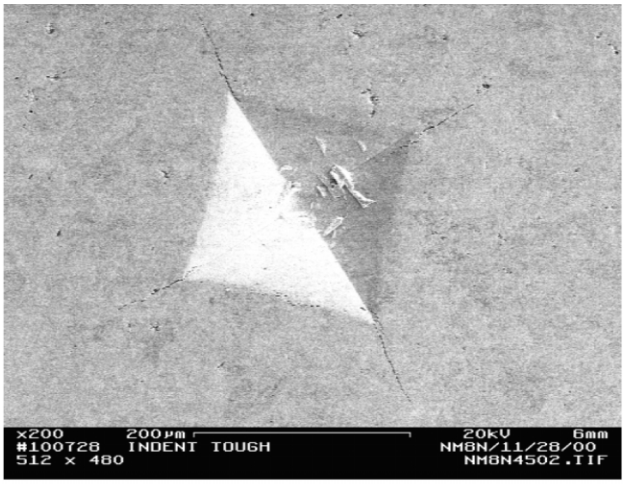

(a)

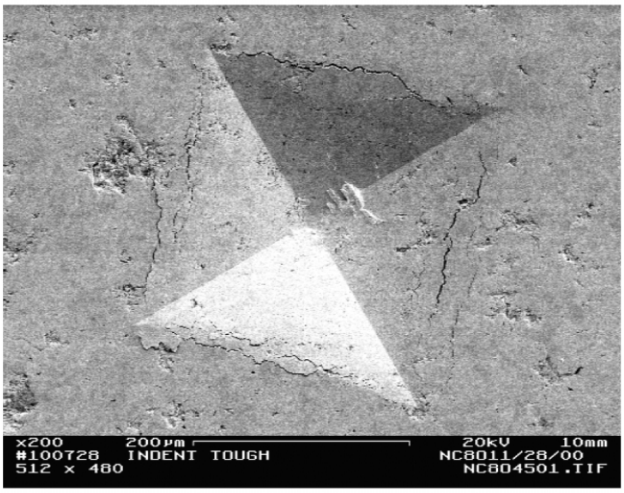

(b)

Fig. 4. Vickers indentation at 45 kg loads on the polished surface of the coatings. (a) Sample NM8N sprayed from multimodal powder in the neutral flame; (b) sample NC8O sprayed from Nanocarb® powder in the oxidizing flame.

semi-empirical equations exist for this purpose. In the present work, we utilize the formula given by Anstis et al. [15]:

$$K_{1C} = 0.016(E/H)^{1/2}P/C^{3/2} \quad (1)$$

where E is Young's modulus, H the hardness, P the load applied to the indenter and C is the length of the crack measured from the center of the indentation. Of our samples, only the ones deposited with a neutral flame exhibited radial cracks (Fig. 4a). In all coatings sprayed with reducing and oxidizing flames, cracks run along the edges of the indents, as shown in Fig. 4b. Therefore, the toughness of these samples cannot be evaluated by Eq. (1). We will see, with the help of the microstructures, that this absence of radial cracks does not indicate a high fracture resistance, but low tensile strength. The increase in surface area created by the indentation and the sharp bend at their edge generates sizeable tensile stresses. This provokes the cracking seen in Fig. 4b.

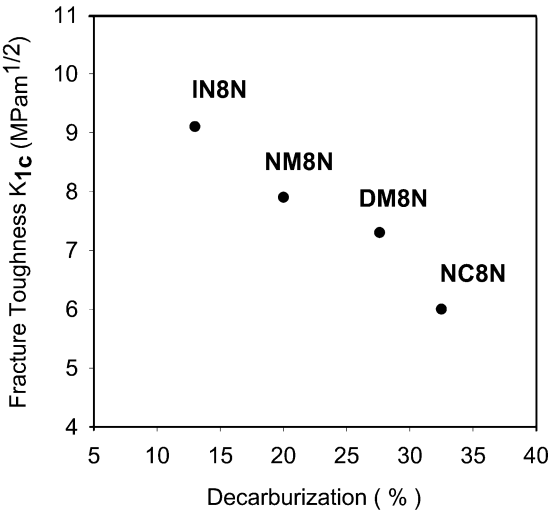

Fig. 5. Surface fracture toughness as a function of decarburization.

Fig. 5 shows the toughness measured at a 45 kg load as it correlates to the amount of decarburization of the coatings sprayed in the neutral flame. Fig. 6 compares the toughness of these samples to their hardness. In classical fracture mechanics, the toughness of a material decreases as the hardness increases, because of crack blunting afforded by plastic deformation. Fig. 6 shows that this relationship does not exist here. In this case, toughness increases rapidly with hardness. The interpretation of these results will be aided by an examination of the microstructure of these coatings.

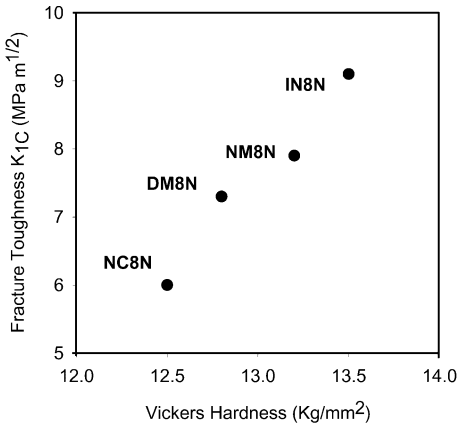

Fig. 6. Fracture toughness as a function of hardness at 1 kg load of the coatings sprayed in the neutral flame.

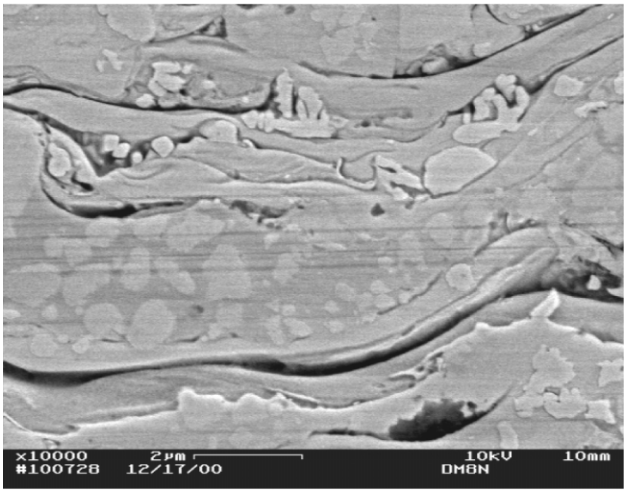

Fig. 7. Cross-section of sample DM8N sprayed from WC–12Co Diamalloy® commercial powders in the neutral condition.

4. Microstructure of the coatings

The microstructures of the coatings were studied on the surfaces and cross-sections by SEM. The surfaces and cross-sections were polished, and then etched. For reasons of space, only the cross-sections will be presented and discussed here. We have found that etching with the Murakami solution provides unclear images because of the presence of reaction products, and that etching in boiling water for 8 min provides much clearer pictures shown in Figs. 7–10.

Before examining the microstructures of our coatings, it will be useful to recall the results of the excellent transmission electron microscopy investigations by Verdon et al. [16] and by Stewart et al. [17]. These authors have presented the following picture of the thermal spray process: while the agglomerated particle is heated in the flame, its cobalt is molten and dissolves a fraction of the tungsten carbide. Since the particle does not reach equilibrium in-flight, it reaches higher temperatures at its surface than at its center. Near its surface, the particle looses carbon to oxidation. Upon impact on the surface, the particle is flattened to form a splat and cools very rapidly. As a consequence, the W- and C-rich cobalt solidifies in nanocrystalline and amorphous form, and precipitates W_2C around the original WC grains [17]. When decarburization is severe, W particles precipitate near the border of the splat. The result is a classic WC–Co structure in the middle of the splat, increasing decarburization towards the splat boundary and an amorphous phase (sometimes with small W precipitates) at the splat boundary. Verdon et al. [16] have also found a 5–10 nm thick, oxygen and carbon-rich, layer separating some splats.

We will now compare the above findings [16,17] with the SEM picture of a water-etched coating, deposited with a commercial powder (Diamalloy 2004), shown in Fig. 7. This particular coating is not state of the art; it has excessive decarburization (28%) and relatively low performance, but it presents the main features revealed by TEM [16,17]. The low magnification of Fig. 7 clearly shows the splat structure. Higher magnification shows the amorphous binder at the borders of the splats. This amorphous phase does not contain WC grains, but the dendrites, described by Verdon et al. [16], are clearly visible. Following Verdon, we think that these dendrites are tungsten. Separate experiments have shown that hot water does not etch tungsten. Between these amorphous phases, we discern the WC–Co structure in the middle of the splats and note the excellent cohesion between WC grains and binder. The shape of the particle on the right bottom corner of Fig. 7 suggests that this is WC surrounded by W_2C. The micrograph also shows 'cracks' between splats. We are not certain that these cracks exist in the coatings as deposited, and are inclined to think that they may result from material dissolution in water. The size and position of these 'cracks' strongly suggest that they correspond to the C and O rich intersplat phase described by Verdon et al. Fig. 7 will serve as a basis for the analysis of the nanostructured coatings deposited in this study. We must emphasize that chemical analysis by EDS in the SEM does not have the spatial resolution, in width and in depth, that would allow us to identify the chemical composition of the different features in these microstructures.

We first analyze the harder coatings deposited in the hotter, neutral, flame. These are shown in Fig. 8. In all three samples, we note that the amorphous bands are much less pronounced than in the conventional sample of Fig. 7, and that the splat boundaries are not as smooth. All three samples contain compact areas of well-bonded WC particles as in Fig. 7, but they also contain areas in which very small pores separate the grains from the binder. The higher decarburization of the multimodal sample NM8N (Fig. 8c) manifests itself in the shape of the grains: they are rounder than in IN8N and many have the scalloped contour of grains surrounded by W_2C [16,17]. It is also noteworthy that the nanostructured grains in the multimodal NM8N have largely disappeared; they were dissolved in the binder. The average grain size and thickness of the binder phase in IN8N is much smaller than in NM8N. We conclude that the increased hardness of IN8N is due to its 'nanostructure', i.e. the small average size of the WC grains and the small thickness of the binder phase.

The microstructure of the Nanocarb® sample NC8N (Fig. 8a), with its extensive decarburization (33%) and the presence of a tungsten peak in its XRD pattern, is quite different from that of IN8N. The low magnification

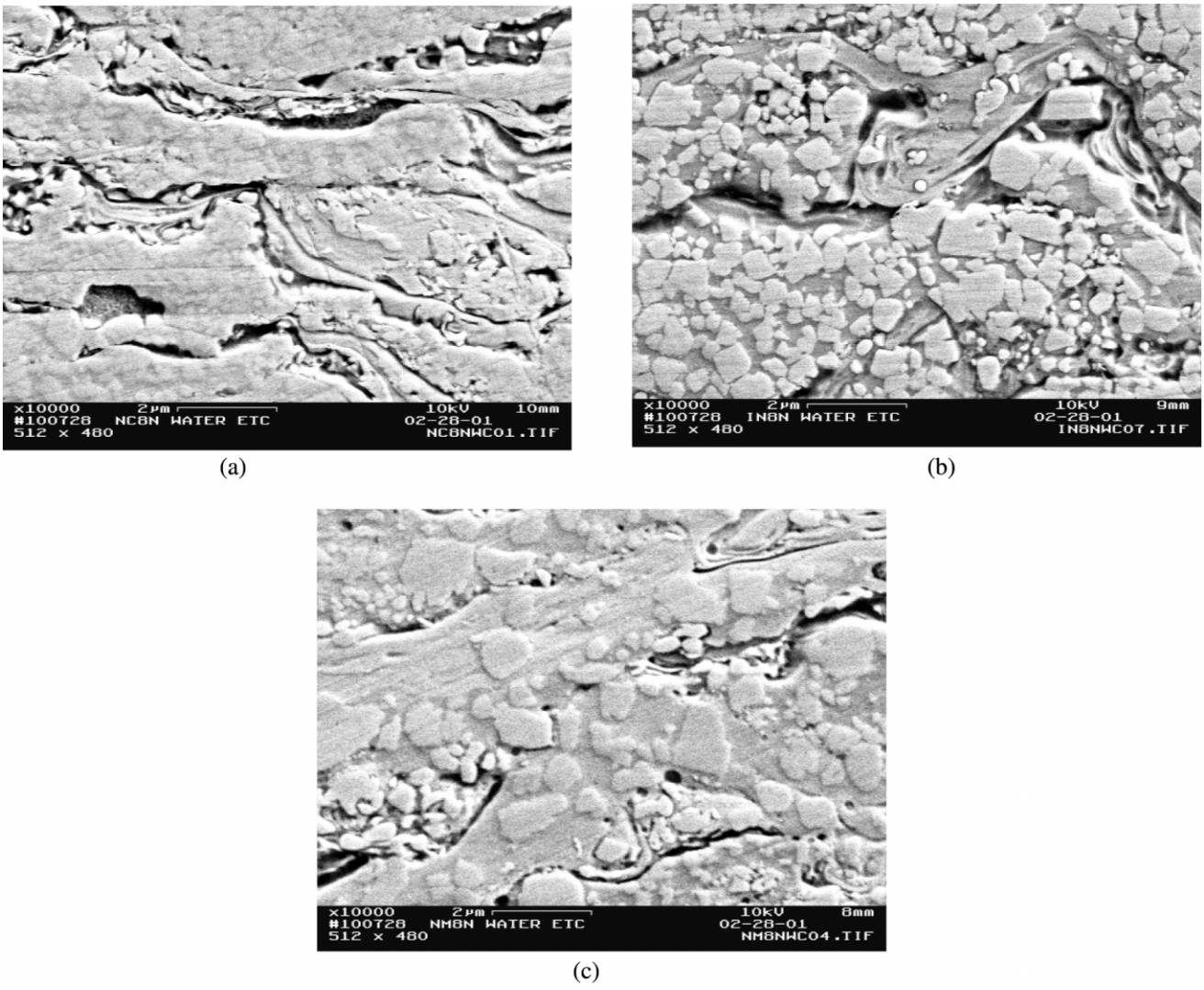

Fig. 8. (a) Cross-section of sample NC8N sprayed from WC–15Co Nanocarb® powders in the neutral condition. (b) cross-section of sample IN8N sprayed from WC–12Co Infralloy® powders in the neutral condition. (c) Cross-section of sample NM8N sprayed from WC–12Co Nanomyte® powders in the neutral condition.

micrographs show that the splat boundaries are more numerous, generally broader, and that they contain rounded precipitates not seen in IN8N and NM8N. The precipitates are attributed to tungsten, as described by Verdon et al. [16]. Clearly, the density of internal flaws in this sample is larger than in the other two.

An overlook of the coatings deposited at lower temperatures and velocities, Figs. 9 and 10, reveals a much higher fraction of area where the WC grains are poorly bonded to the binder. Also, the amount of microporosity is much higher. Such samples also present low tensile strength, which accounts for the cracking along the edges of the indentations (Fig. 4) instead of the formation of radial cracks. As a rule, the samples in the reducing flame show a higher hardness than those sprayed with the oxidizing jet. We attribute this to the larger particle velocity on impact. This manifests itself in the slightly lower porosity of these samples (Fig. 10 compared to Fig. 9). In accordance with Fig. 2, which shows that the hardness of the Nanocarb® samples NC8R and NC8O is somewhat higher than that of the other materials deposited at low temperatures, the microstructure of these samples is less porous and better bonded because of their very fine grain size. The multimodal Nanomyte® samples deposited with reducing and oxidizing flames exhibit small bands of well-bonded WC–Co, and a large fraction of the material with poor bonding where micropores separate the grains from the binder.

The porosity of the coatings was measured on the polished surface with an Olympus optical microscope at 500× magnification according to ASTM standard [B276]. The amount of porosity was calculated from a selected area by Scion® image software, as listed in

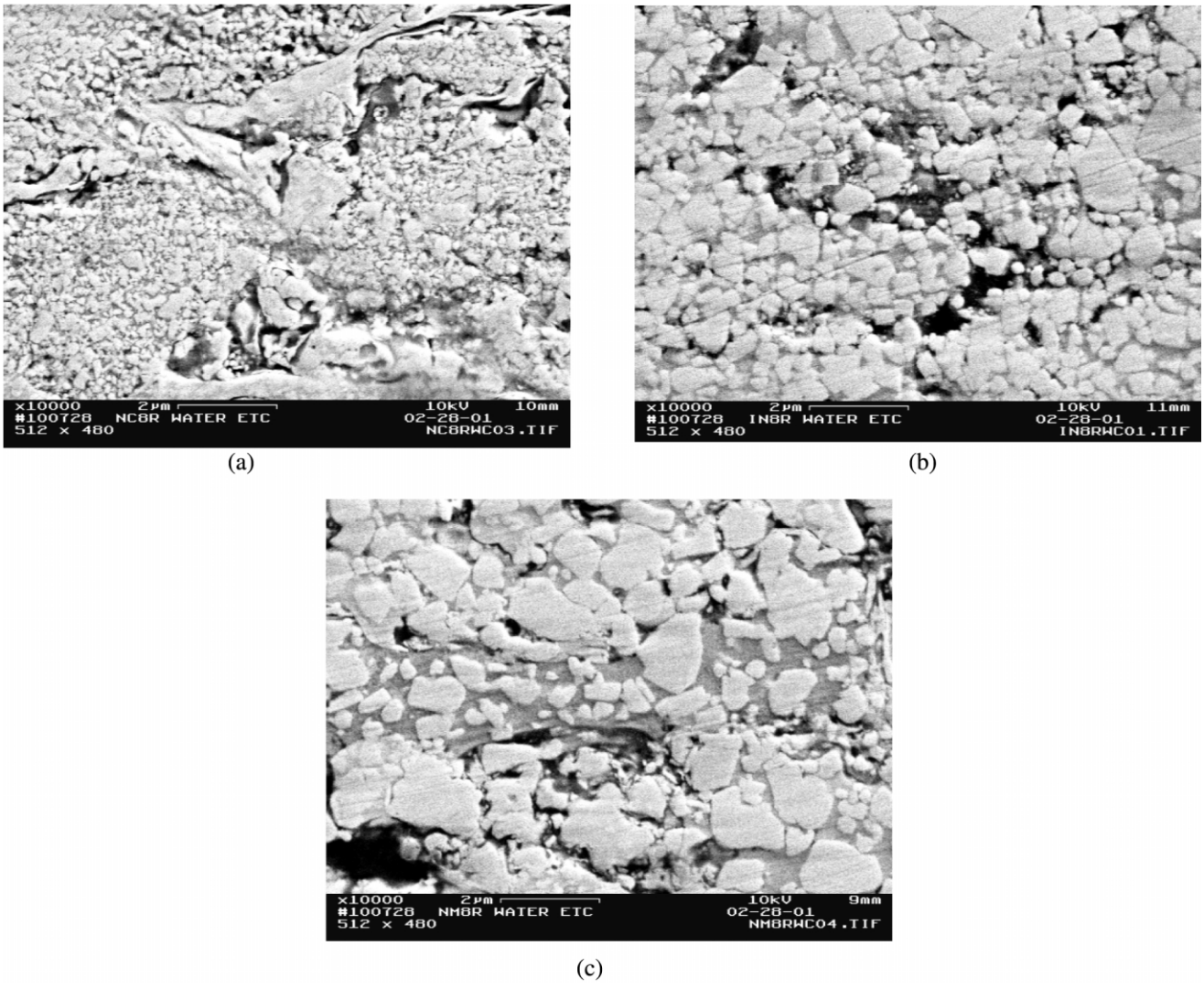

Fig. 9. (a) Cross-section of sample NC8R sprayed from WC–15Co Nanocarb® powders in the reducing condition. (b) cross-section of sample IN8R sprayed from WC–12Co Infralloy® powders in the reducing condition. (c) Cross-section of sample NM8R sprayed from WC–12Co Nanomyte® powders in the reducing condition.

Table 1. We note that these values are all below 3%. Since this porosity was measured in an optical microscope with 500× magnification, it only represents pores that have a size of at least 2 μm. High resolution SEM show that the pores relevant to mechanical properties are extremely small and are not reflected in the values of Table 1.

5. Discussion of structure and mechanical properties

Before going on to the tribological performance of the coatings, it is useful to review their structure and mechanical properties. The hardness of the coatings deposited in the hot, neutral flame (HV 1300) approaches that of sintered WC–Co cermets. Low hardness of coatings is usually attributed to porosity. The porosity reported in Table 1, and measured with the optical microscope, is too low to account for the low hardness of the coatings deposited with oxidizing and reducing flames. The microstructure of these samples suggests that flaws such as weak bonding between WC and binder, the resulting nanometer sized pores, and low adhesion between splats determine the hardness of the coatings. This also explains the local variations in hardness we have observed.

In sintered WC–Co, we had found that the toughness decreases as hardness increases. This relationship is observed for most materials and is attributed to plastic deformation at crack tips that increases fracture energy. In the sprayed coatings presented here, the same flaws that decrease the hardness also decrease the tensile strength and accelerate crack growth. Therefore, toughness and hardness increase together, as shown in Fig. 6. Since the brittle W_2C grains are very small, and usually

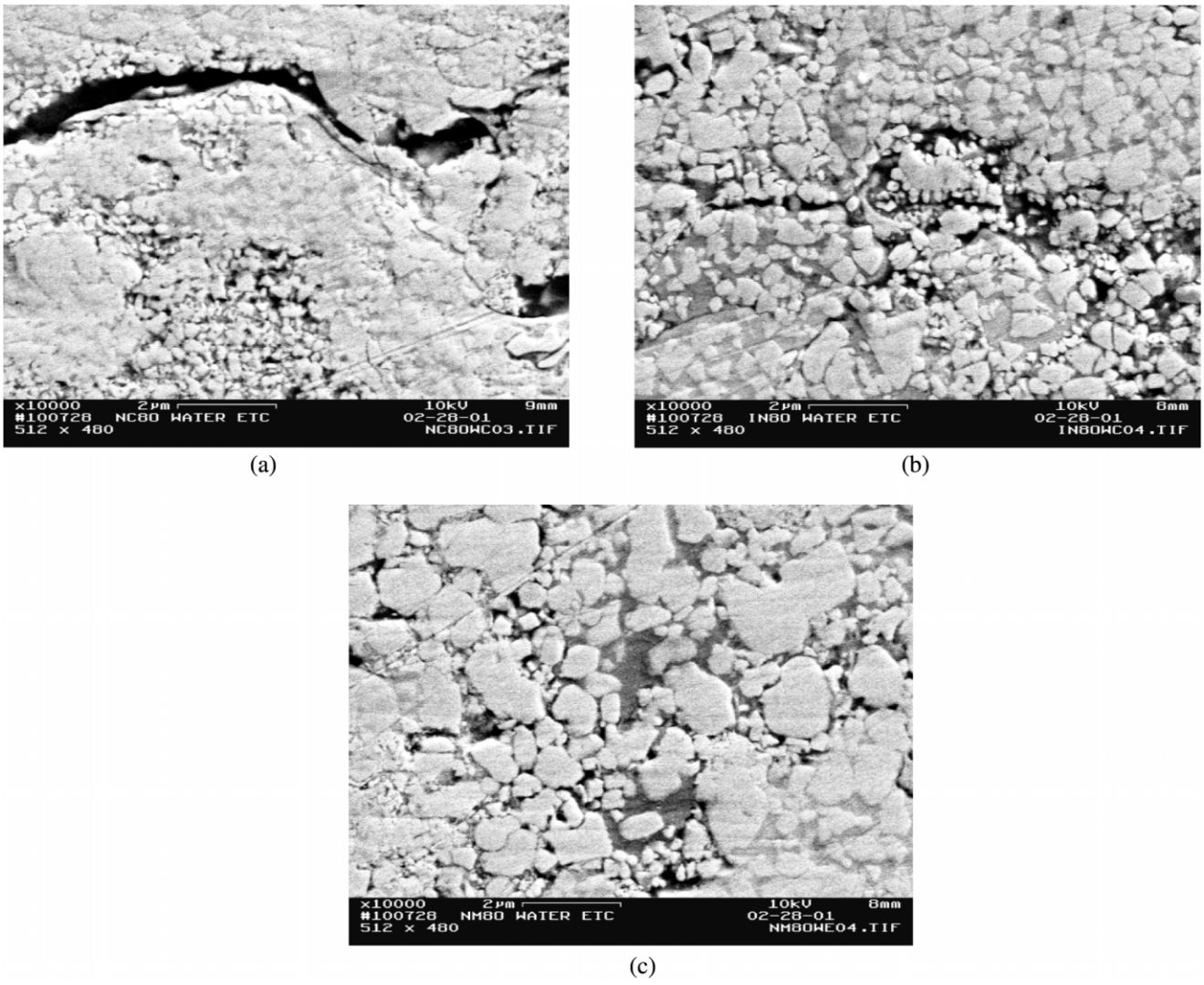

Fig. 10. (a) Cross-section of sample NC8O sprayed from WC–15Co Nanocarb® powders in the oxidizing condition. (b) Cross-section of sample IN8O sprayed from WC–12Co Infralloy® powders in the oxidizing condition. (c) Cross-section of sample NM8O from WC–12Co Nanomyte® powders sprayed in the oxidizing condition.

attached to WC, we conclude that they do not contribute measurably to the brittleness of the coatings. The brittleness of these samples results from poor adhesion between the splats, WC–W_2C grains, and binder.

The proprietary grain growth-inhibiting additive in the IN powder has a large effect on the microstructure of the coatings. Grain growth inhibitors act by preventing the diffusion or evaporation of material from small grains to larger ones. By preventing the diffusion of W and C, the inhibitor also prevents the enrichment of the binder phase in these elements. Suppression of W and C dissolution in Co also decreases the amount of wetting between the WC grains and the binder and produces the nanopores that were observed in Figs. 9 and 10. It also explains the fact that the WC grains in all IN samples retain their angular shapes and straight boundaries.

By comparing the microstructures of NM8N and IN8N, we conclude that the hardness of NM8N is limited by the relatively thick binder phases that result from the dissolution of the nanosized WC, and that the hardness of IN8N, despite its smaller WC and thin binder phase, is limited by the reduced cohesion between WC and the binder. This distinction is important in understanding the abrasive wear resistance of these samples.

6. Wear

6.1. Wear tests

Two types of wear tests were performed: very short tests were used to observe isolated wear mechanisms on

virgin surfaces and long test served to determine quantitative wear rates.

Sliding wear tests were conducted in laboratory atmosphere with a ball-on-disk tribometer in which a WC–Co coated steel disk slid, without lubrication, against a commercial Si_3N_4 ball of 1/4 inch diameter. The surfaces of the WC–Co coatings were polished to $R_a < 0.04$ μm in the same manner as for hardness measurements. The sliding speed was 58 mm/s and the load 9.8 N. The diameter of the traveling circle of the pin on the disk was 8.5 mm. The volume of material removed from the coating was determined by measuring the cross-section of the wear scar with a profilometer at six positions and averaging. The wear of the silicon nitride was measured from the size of the wear flat on the ball. The long term tests ran to a distance of 5000 m or 190 000 rotations of the disk.

Abrasion tests were performed on a ML-100 pin-on-disk tribometer in ambient temperature and humidity. WC–Co coated steel pins with 8×8 mm^2 area were slid under a load of 2–17 N against disks of SiC abrasive bonded to paper. The abrasive was LECO 120 GRIT (106 μm) plain abrasive with a hardness of $Hv_{0.1}$ 2600. In the long-term abrasion tests, the samples moved in a spiral on the abrasive disk in order to encounter fresh abrasive during the whole sliding distance of 38 m. A new abrasive disk was used for each run. The loss of material was determined by weighing the samples before and after the tests after ultrasonic cleaning.

6.2. Presentation of the wear data

We have verified experimentally that the amount of material removed in sliding and abrasive wear is proportional to the normal force on the ball and the distance slid. The volume of material removed is expressed as

$$V = kPs/H \tag{2}$$

where V is the volume lost to wear, P the normal force on the slider (the load), s the sliding distance, H the hardness and k is the dimensionless wear coefficient. From this equation, we define the wear rate

$$W = V/Ps = k/H \tag{3}$$

which is expressed in mm^3/Nm.

We can define the sliding wear resistance as

$$R = 1/W = Ps/V = cH. \tag{4}$$

The dimensionless factor $c = 1/k$ is the wear resistance coefficient. The coefficients k and c express influences other than hardness on the wear of the coatings.

The above equations are equally valid for sliding and abrasive wear. We shall differentiate the two by writing W_{sl}, R_{sl}, c_{sl} and k_{sl} for sliding and W_{ab}, R_{ab}, c_{ab} and k_{ab} for abrasion.

In order to compare sliding and abrasive wear, the latter is expressed in mm^3/Nm. A density of 14 g/cm^3 is used to transform the mass into volume. This is the density of compact, sintered, materials. We are aware that the density of the coatings is usually lower because of porosity. The latter is difficult to measure accurately on coatings. The use of $\rho = 14$ g/cm^3 then expresses abrasive wear in terms of mass removed, rather than dimensional modification.

The wear rates are obtained in absolute values of mm^3/Nm. We must recall that these values are not universal but are valid for unlubricated sliding against silicon nitride at moderate velocities in air and at room temperature. Very different wear rates would be obtained in different conditions such as lubrication, extreme environments, high temperatures. The latter would result for instance from rapid sliding at high loads. Similarly, the abrasive wear rates are valid in abrasion by 120 grit silicon carbide; different grit sizes and abrasive materials would produce different values. Nevertheless, these values allow a meaningful comparison between different materials and deposition methods.

6.3. Results and discussion of wear

When plotting the quantitative wear results, we choose to represent the wear resistance R (Eq. (4)) because it shows the influence of hardness in a linear fashion. Fig. 11 shows the sliding and abrasive wear resistance as a function of the hardness of the coatings according to Eq. (4). We note that the sliding wear resistance is at least 4 orders of magnitude higher than the abrasion resistance. The sliding and abrasive wear resistances increase roughly with hardness, but sizeable deviations from a simple linear relationship indicate that other material properties are influential. These will be expressed later by the wear coefficients k and c.

In Fig. 11, we plot the average values of hardness and the sliding wear resistance. In reality, the hardness varies considerably over the surface of the sample. A detailed investigation [14] has shown that the local wear resistance on a given sample is proportional to the local hardness. Therefore, the average values of wear rate plotted against average hardness are representative of the properties of the coatings. In the case of abrasion, only the overall wear rate can be measured, so that the average hardness is again the representative quantity.

Microscopic observation of the wear tracks provides further information about the wear mechanisms and their relation to the material properties of the coatings. Observations of wear tracks at short sliding or abrasion

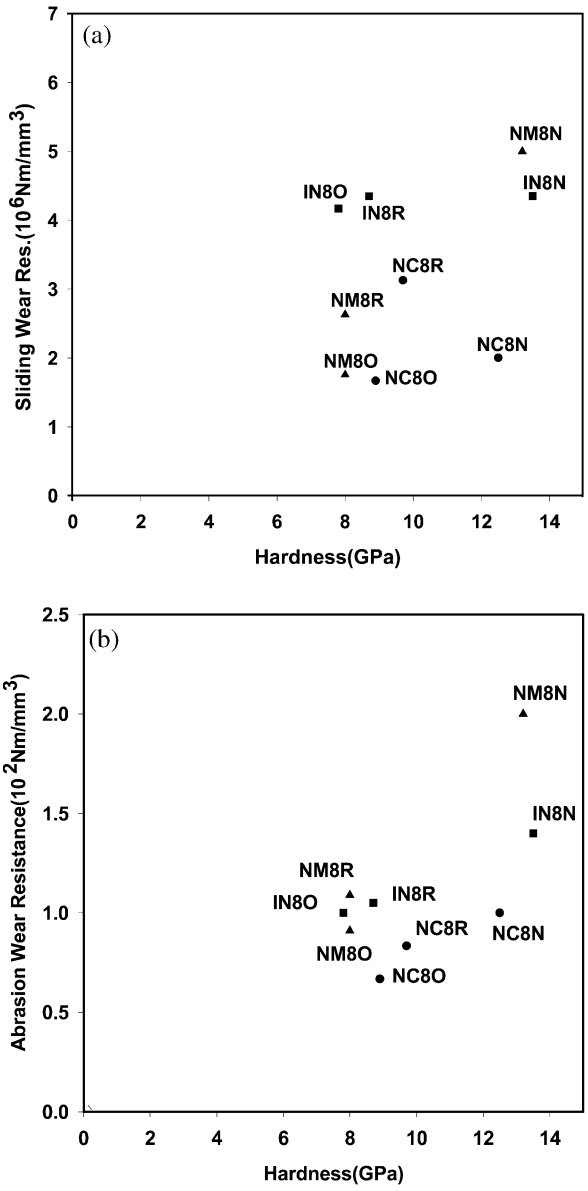

Fig. 11. Sliding and abrasion wear resistance of nanostructured WC–Co coatings as a function of their hardness.

distances provide the clearest information because they show individual wear events.

We first analyze the wear of the materials deposited at high flame temperatures since they provide the best performance. The short abrasive wear grooves of NM8N, IN8N and NC8N are shown in Figs. 12–14. Abrasion in NM8N (Fig. 12) consists of ductile cutting, similar to what happens in a metal. We note that the groove is smooth, which indicates that the abrasive cuts through the larger WC particles as well as through the binder. Apart from the cutting, there is little evidence of lateral plowing. The dark spots in the figure represent pores. The groves in IN8N (Fig. 13a) present evidence of weaker bonding between the WC grains and the binder. There is additional material removal in lateral plowing by separation of the WC grains. The difference in the shapes of the wear particles is striking: the wear particle of IN8N shows clear evidence of separation of platelets which is absent in NM8N. In sample NC8N, Fig. 14, which is severely decarburized, we observe a pit in the ductile groove; its bottom is smooth, without trace of cutting. The morphology of this pit strongly suggests that it was caused by the removal of material from a weak interface. If we refer to the microstructure of this sample (Fig. 8a), we conclude that this interface is a splat boundary and that the pit was formed by the lifting of a poorly bonded splat fragment.

The sliding wear tracks of the same coatings at short distances (Figs. 15–17) show features that are compatible with those in the abrasion grooves. (In these micrographs, the dark 'clouds' represent silicon nitride wear particles from the ball.) The multimodal coating NM8N (Fig. 15) is characterized by wear of the binder, leaving the larger WC grains to stand proud. Coating IN8N (Fig. 16) exhibits small, shallow, pits that are caused by the breaking out of individual grains, especially at the pit boundary, where local contact stresses are enhanced. The nanostructured NC8N (Fig. 17), which suffered 33% decarburization, exhibits a large pit. Its morphology is similar to that on the abrasion groove Fig. 14. We conclude that this pit results from the detachment of a splat as in abrasion. Outside of the pits, this coating also shows evidence of wear of the binder, similar to coating NM8N (Fig. 15).

We have seen that adhesion between the WC grains and the binder is weak in coating IN8N because of the additive and in all the samples deposited with low flame temperature. This feature explains the abrasive and sliding wear of sample IN8N. We have also found that

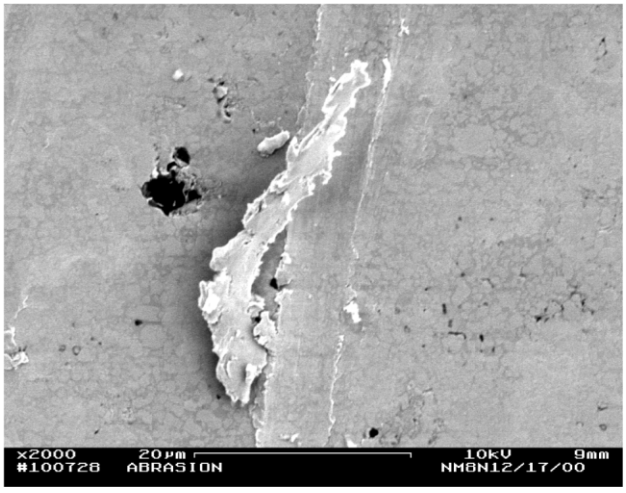

Fig. 12. SEM micrograph of short abrasion wear track of WC–Co coating NM8N deposited with multimodal powder Nanomyte using DJ2700 gun with hot, stoichiometric, flame.

(a)

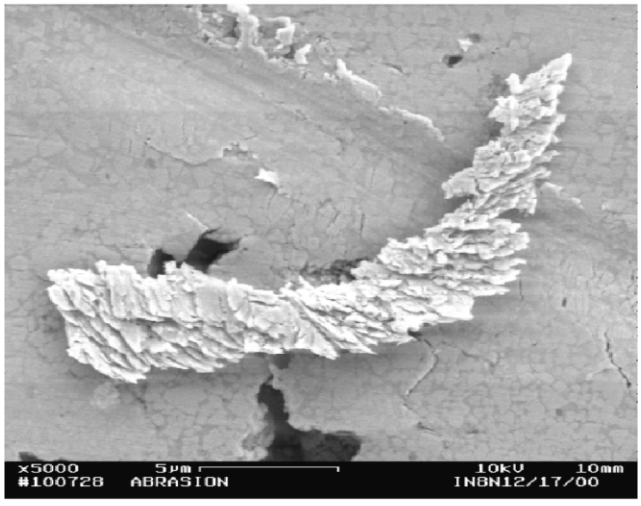

(b)

Fig. 13. SEM micrograph of short abrasion wear track of WC–Co coating IN8N deposited with Inframat powder (WC size 200 nm) containing an additive using DJ2700 gun with hot, stoichiometric, flame. (a) Abrasion groove showing grain separation. (b) Abrasive wear particle.

the adhesion between splats is weak when the degree of decarburization is high. This explains the formation of pits by splat removal observed with sample NC8N. In coating NM8N, the sliding wear is limited to attrition of the binder and wear of the WC grains and abrasion takes the form of ductile cutting, in agreement with the properties of this material described above.

The same relationships between material properties and wear mechanisms are found in the long wear tests. The sliding wear tracks after long sliding tests of 5000 m are shown in Fig. 18. In the highly decarburized coating NC8N, Fig. 18a, we discern a high density of pits, 10–30 μm in diameter and 3 to 5 μm deep (the latter measured with an optical microscope). The bottoms of these pits are smooth as in Fig. 17; they are obviously the amorphous boundaries of splats we have described in Section 7. Coating NC8O has a similar wear track but with more pitting. We conclude that wear of these samples consists of the removal of entire splats in addition to the attrition of WC grains. We compare this track with that of coating IN8R, which has experienced very low decarburization, Fig. 18b. Low magnification shows a smaller density of pits and high magnification reveals that their bottom is granular. These pits do not represent lifting of splats, but are original pores in the samples that have been enlarged by loss of grains at their border due to high local contact stresses. Such porosity exists in all samples deposited at low

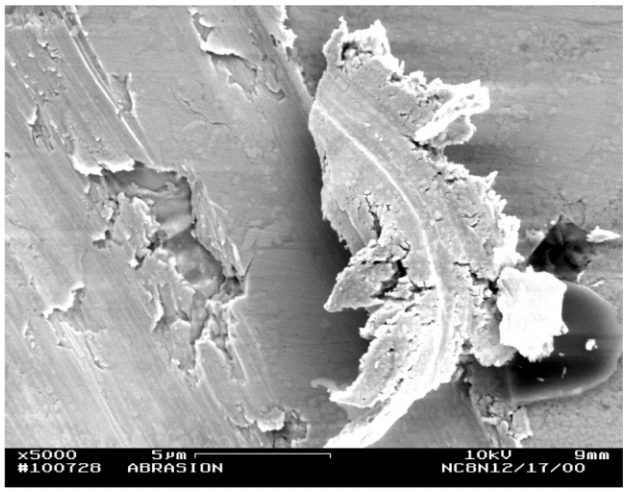

Fig. 14. SEM micrograph of short abrasion wear track of WC–Co coating NC8N deposited with Nanocarb powder (WC size 70 nm) using DJ2700 gun with hot, stoichiometric, flame.

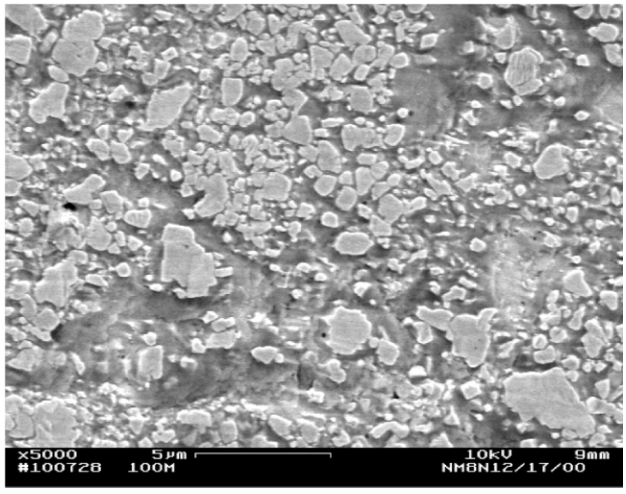

Fig. 15. SEM micrograph of short (10 m) sliding wear track of WC–Co coating NM8N deposited with multimodal powder Nanomyte using DJ2700 gun with hot, stoichiometric, flame.

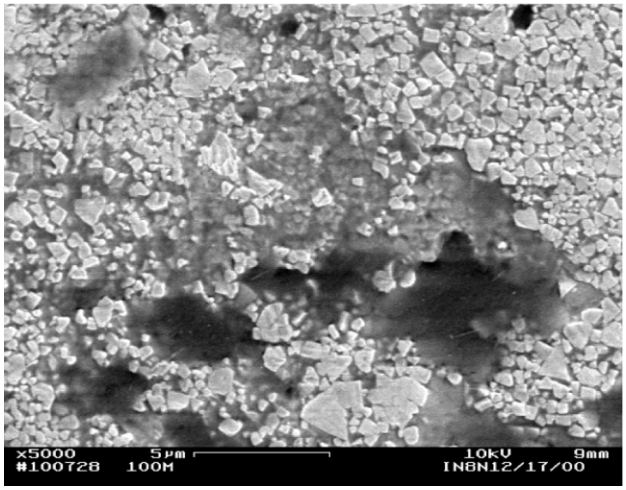

Fig. 16. SEM micrograph of short (10 m) sliding wear track of WC–Co coating IN8N deposited with Inframat powder (WC size 200 nm) containing an additive using DJ2700 gun with hot, stoichiometric, flame.

temperature and in coating IN8N containing the additive. The wear track of coating IN8O is similar to that of IN8R. The much harder coating IN8N does not have the grooves but contains a number of pits similar to those of NC8N because of its 13% decarburization.

After long abrasion tests the appearance of the surfaces reveals the influence of material properties in a similar way. Fig. 19 shows two extreme examples. The hard, ductile coating NM8N shows smooth and shallow abrasion grooves that reflect the hardness and ductility of this sample. Coating NC8O exhibits deep grooves because of its low hardness and a rough surface caused by the removal of splats.

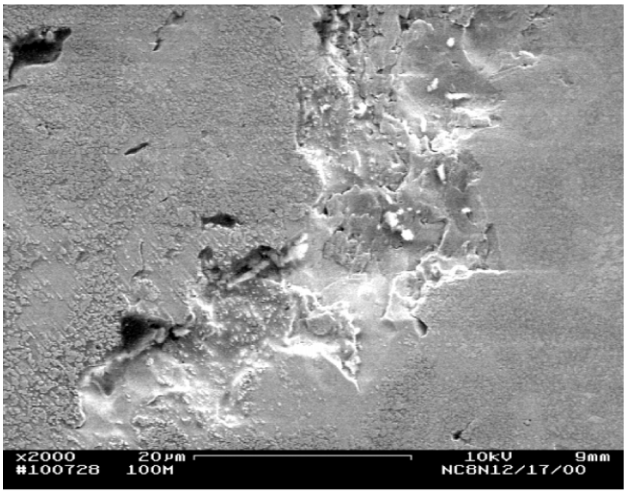

Fig. 17. SEM micrograph of short (10 m) sliding wear track of WC–Co coating NC8N deposited with Nanocarb powder (WC size 70 nm) using DJ2700 gun with hot, stoichiometric, flame.

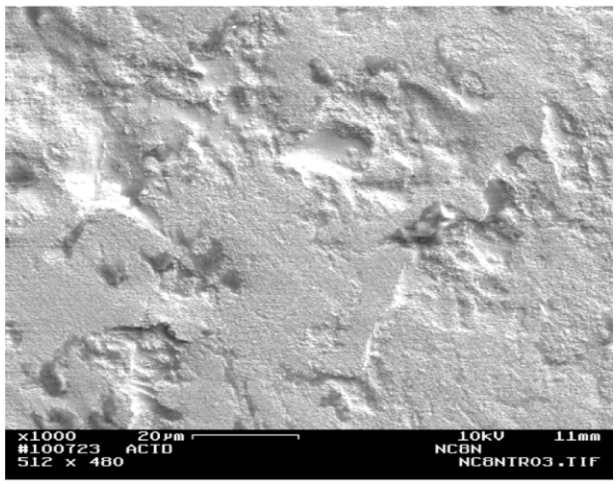

(a)

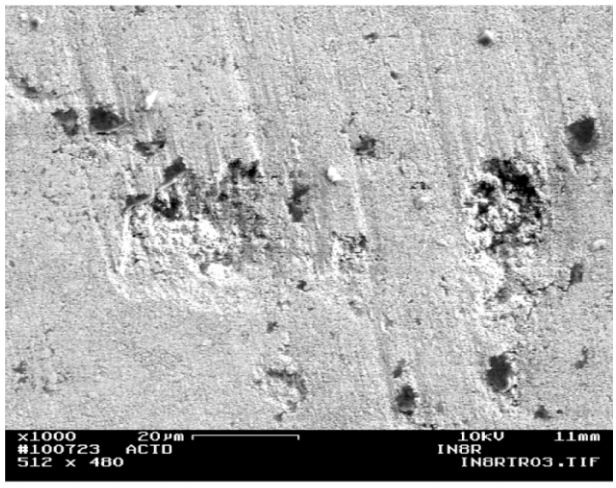

(b)

Fig. 18. SEM micrographs of wear tracks in WC–Co coatings after 5000 m sliding distances at 9.8 N load. (a) Coating NC8N deposited with Nanocarb powder (WC size 70 nm) using DJ2700 gun with hot, stoichiometric, flame; (b) coating IN8R deposited with Inframat powder (WC size 200 nm) containing an additive using DJ2700 gun with cool reducing flame.

The observations of the wear tracks show that sliding wear of the WC–Co coatings consists of three mechanisms: the wear of individual WC grains, the falling out of grains in grooves or around native pores, and the lifting of entire splats in decarburized samples where the splat boundaries are weak. These three mechanisms operate in all samples to different degrees, depending on the material properties that result from the particular powders and processing parameters. Wear of the WC grains undoubtedly exists; in sintered WC–Co composites, we have seen that such wear produces polished WC grains [4]. In the present coatings, it is impossible to distinguish experimentally the parts played by the falling out and the wear of the WC grains so that we are reduced to lumping them together as grain attrition.

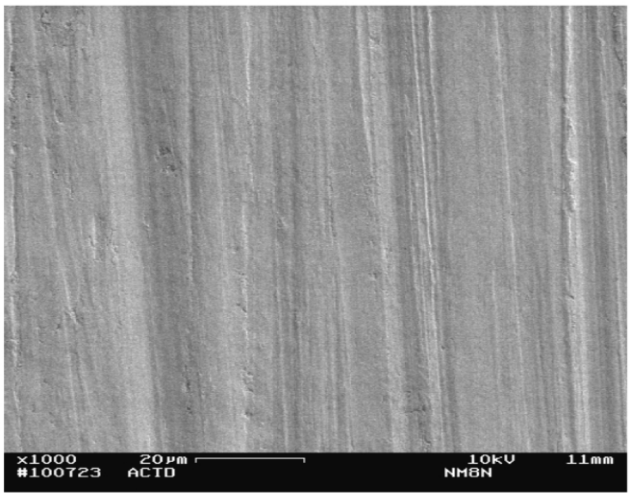

(a)

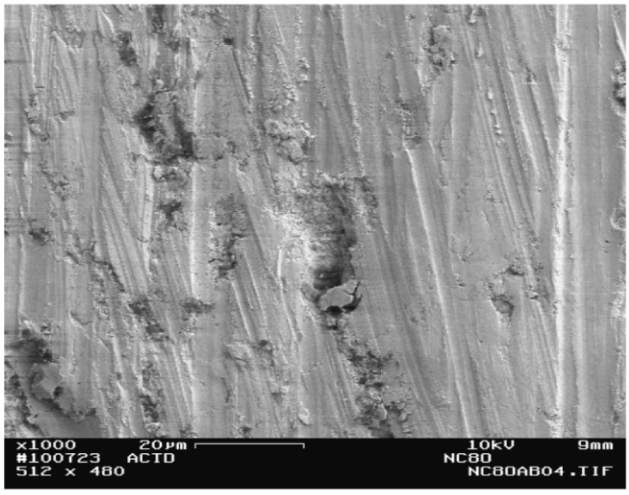

(b)

Fig. 19. SEM micrographs of abraded surfaces after long abrasion test (38 m at 17 N load). (a) Coating NM8N deposited with multimodal powder Nanomyte using DJ2700 gun with hot, stoichiometric, flame. (b) Coating NC8O deposited with Nanocarb powder (WC size 70 nm) using DJ2700 gun with a cool, oxidizing, flame.

Earlier work has revealed that decarburization has a pronounced effect on the wear of the coatings [5–12]. In order to examine this effect, we present the wear coefficients k_{sl} and k_{ab} in Fig. 20 as a function of the degree of decarburization. We recall that these coefficients represent the departures from the simple proportionality of wear resistance to hardness (Eqs. (2)–(4)).

We draw the following conclusions:

(1) The wear coefficients are roughly proportional to the amount of decarburization, designated as d, and can be expressed empirically as

$$k = k_o(1+\alpha d).$$

(2) In sliding wear, as in abrasion, the wear coefficient of coating NM8N, with the multimodal structure, lies significantly below the curve describing the other coatings. We attribute this to the excellent adhesion of the large WC grains to the Co binder. Fig. 13 shows that early sliding wear consists mostly of the wear of the binder; the WC grains stand proud of the surface and Fig. 12 shows that early abrasion consists of ductile cutting as in metals. All other coatings with the exception of NC8N have a reduced WC-binder adhesion, either because of the additive or because of low flame temperature, therefore the k_o values for sliding and abrasion on Fig. 20 correspond to materials with relatively poor adhesion between WC and binder.

(3) In accordance with Fig. 11, the effect of decarburization is more pronounced in sliding wear than in abrasion.

$$k_{sl} = 1.75\times10^{-6}(1+7.8d) \quad (5)$$

$$k_{ab} = 0.076(1+2.3d). \quad (6)$$

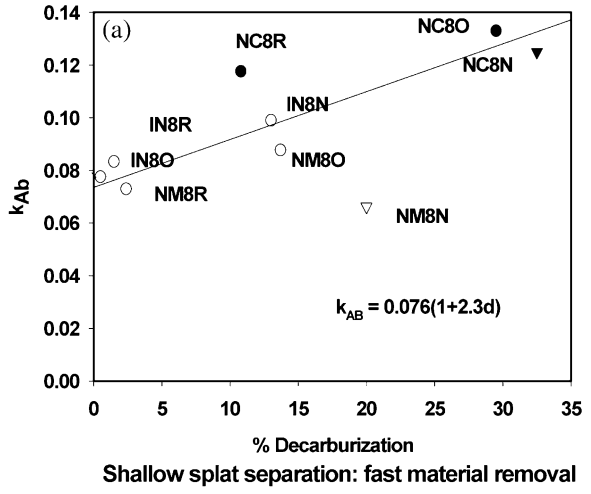

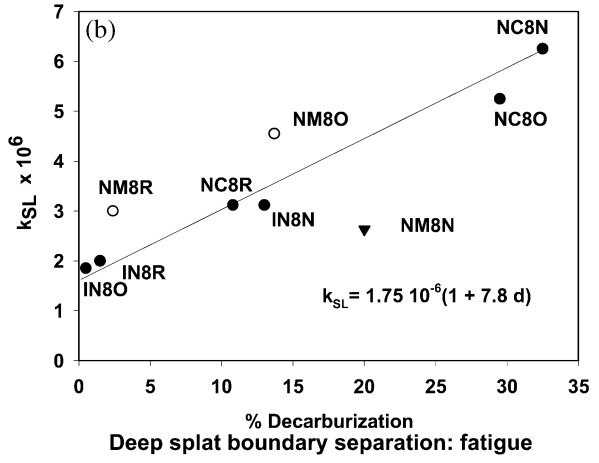

Fig. 20. Sliding and abrasive wear coefficients k_{sl} and k_{ab} (defined in Eq. (2)) of the coatings as a function of the degree of decarburization.

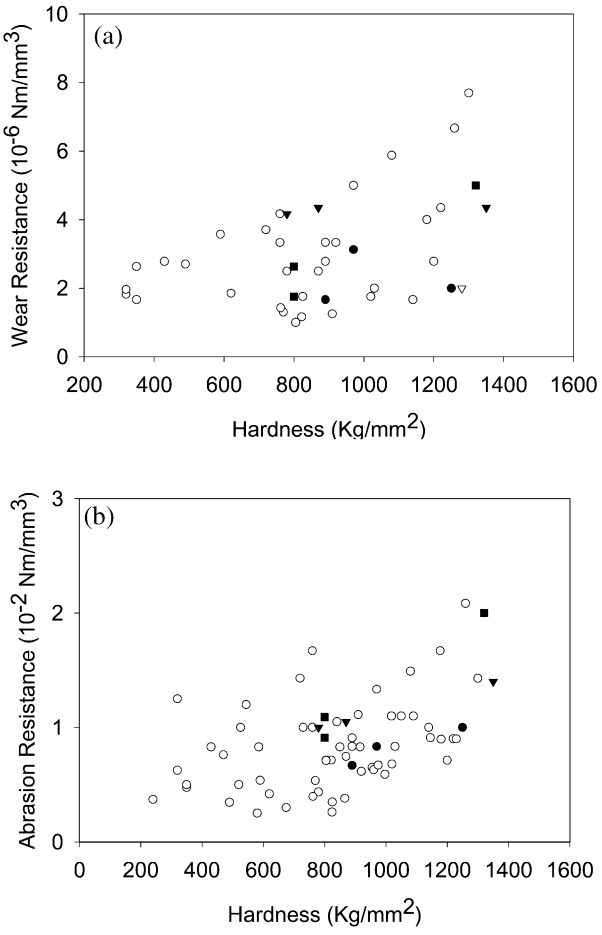

Fig. 21. Comparison of the tribological performance of the coatings with that of other WC–Co coatings deposited with commercial and nanostructured powders by HVOF or plasma and tested under identical conditions (from Ref. [7]). Open circles: form Ref. [7]; full circles: Nanocarb coatings; triangles: Inframat coatings; squares: Nanomyte coatins.

This difference is attributed to differences in wear mechanisms. We have already noted that sliding wear is four orders of magnitude slower than abrasive wear. In our sliding experiments, the sample makes more than 100 000 turn against the ball before a depth of 1 μm is removed. The many passes of the slider fatigue the weak splat boundaries. In addition, the larger extension of the sliding contact causes subsurface stresses to penetrate deeper under the surface than in abrasion. During the much more rapid abrasive wear, the splat boundaries are subjected to much less weakening by fatigue, and splats are removed only when their boundaries are at shallow depths and there is little lateral support for the splat. Consequently, pits due to splat removal are larger and deeper in sliding than in abrasion and the effect of decarburization on wear is more pronounced in sliding.

(4) We note in Fig. 20 that the sliding wear coefficient of NM8R and NM8O is higher than for the other materials and in abrasive wear, the wear coefficients of the Nanocarb samples NC8R and NC8O are higher than those of the other samples. We do not have any experimental evidence that could explain these differences.

The important question is how the tribological performance of these coatings compares with that of WC–Co coatings deposited with commercial powders and standard methods. We have previously examined the sliding and abrasive wear resistance of a large number of coatings that were deposited by various techniques, including standard commercial powders and guns [7]. Fig. 21 compares the performance of all these coatings (in open circles) with that of the coatings studied here. The open circles represent the coatings of Ref. [7] and the black symbols are a repeat of the data of Fig. 11. We observe that the abrasion resistance of sample NM8N (full square) is as good as that of the best samples studied. In sliding wear, the wear resistance of samples IN8N, IN8R, IN8O and NM8N is surpassed by only three coatings which were deposited with DJ2700 guns and commercial powders in research laboratories.

In sliding wear, one must consider not only the wear of the material investigated, but also the wear it inflicts on the body on which it slides. We have measured the wear of the silicon nitride balls sliding against the coatings and present the results in Fig. 22. The Infralloy® and Nanocarb® samples cause relatively little wear of silicon nitride. This is easy to understand: the small WC grains and the fewer and shallower pits give these coatings a smooth worn surface that causes little abrasion of the ceramic. Thus, for a system where both sliding partners are required to present good wear

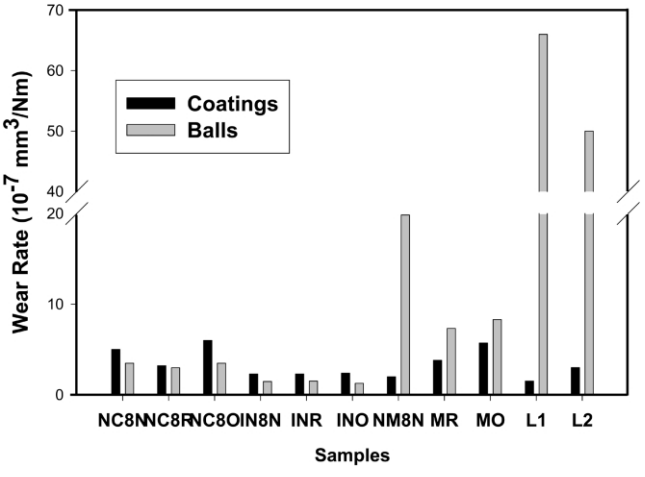

Fig. 22. Comparison of the sliding wear rates of the WC–Co coatings with those of the silicon nitride balls against which they slid. Samples L1 and L2 are coatings deposited with commercial powder Metco 2004 with the same Metco DJ2700 guns as the others. Sample denominations IN8R, IN8O were abridged to INR and INO, samples NM8R and MN8O were abridged to MR and MO for legibility.

resistance, coatings made from the Inframat powder with the additive give the best performance. It is of practical interest that the wear performance of the Inframat coatings is quite insensitive to the spray method. IN8N may be the preferred choice because of its hardness. Coating NM8N is very destructive on the silicon nitride because of its rough surface consisting of large hard WC grains standing proud of the binder. We also show the WC–Co and silicon nitride wear of two coatings of Fig. 21 that present higher sliding wear resistance than the Inframat and NM8N coatings. We recall that these were deposited from commercial powders with micrometer size WC grains. These coatings inflict even higher wear on the silicon nitride ball. We conclude that nanostructured coatings have the advantage of causing relatively mild wear in the materials against which they slide.

7. Conclusions

This examination has allowed us to gain insight into the relative importance of flame parameters, WC grain size, and agglomerate properties in determining the structure, hardness and toughness of WC–Co coatings. In particular, we have learned that:

1. It is possible to deposit nanostructured WC–Co coatings with superior tribological performance.
2. The hardness and the toughness of the coatings are limited by flaws inherent in the spray process, namely poor adhesion between WC grains and binder, and poor adhesion between splats. Therefore the hardness and toughness of the coatings increase together, in opposition to the behavior in most materials.
3. The hardest and toughest coatings are obtained with a hot, neutral flame and powders that minimize decarburization. This is attributed to sufficient melting of the agglomerates and limited reaction between WC and binder.
4. Decarburization results in the formation of W_2C and in the loss of inter-splat adhesion, which is responsible for the degradation of mechanical properties; the W_2C grains are too small to contribute effectively to fracture.
5. Wear mechanisms in sliding consist of continuous wear of binder and WC grains, removal of entire WC grains and removal of splats. Wear in abrasion consists of ductile cutting, removal of grains and removal of splats or their fragments. These mechanisms operate simultaneously and are caused by structural defects introduced by the spray process.
6. Decarburization increases wear by removal of splats or splat fragments because it produces weak inter-splat boundaries. This wear mechanism is important in sliding wear, but less so in abrasive wear. This is attributed to the low sliding wear rate which favors fatigue of the splat boundaries.
7. Removal of grains is caused by weak WC-binder adhesion. The latter results from low flame temperature and from the grain-growth inhibitor additive in the ‘near-nano’ powder.
8. A grain-growth inhibitor has a strong influence on the microstructure and other properties of the coatings. By preventing WC dissolution in the binder, it not only maintains very small grains, but also maintains their original shape; it is effective in retarding decarburization but decreases the cohesion between WC and binder.
9. It is essential to prevent a large surface to volume ratio in the agglomerates and in the grains of the powder to achieve desirable mechanical properties.
10. Superior abrasion resistance is obtained from coating NM8N deposited at high flame temperature with the multimodal (Nanomyte) powders.
11. Superior sliding wear resistance is obtained from coatings deposited with near nano powders containing an anti-growth additive (Inframat). These coatings are insensitive to the details of the coating process and therefore to the skill of the operator. The multimodal coating NM8N has even better sliding wear resistance, but inflicts heavy wear on the counter-body.
12. Nanostructured WC–Co coatings inflict low wear on the body against which they slide (silicon nitride).
13. The high temperatures of the hybrid spray gun produced hard coatings with superior hardness and wear resistance. Reducing the flame temperature in order to reduce decarburization does not provide better wear resistance.

Acknowledgments

Support for this by the Office of Naval Research, under Grant N00014-00-1-0685, is gratefully acknowledged. The authors express their gratitude to Professor Bernard Kear, Mr Robert Rigney, Dr Ganesh Skandan, and Dr Vasudevan Asuri for many helpful discussions. They thank Miss Michelle Gerritsen for editorial work on the manuscript.

References

[1] L.E. McCandlish, B. Kear, B.K. Kim, J. Mater. Sci. Technol. 6 (1990) 953–960.
[2] K. Jia, T.E. Fischer, G. Gallois, J. NanoStructured Mat. 10 (1998) 875–891.
[3] K. Jia, T.E. Fischer, Wear 200 (1996) 206–214.
[4] K. Jia, T.E. Fischer, Wear 203–204 (1997) 310–318.
[5] S. Usmani, S. Sampath, Tribol. Trans. 40 (3) (1997) 470–478.
[6] D.A. Stewart, P.H. Shipway, D.G. McCartney, Wear 225–229 (1999) 789–798.

[7] Y. Qiao, Y.R. Liu, T.E. Fischer, J. Thermal Spray Technol. 10 (2001) 118–125.
[8] G. Skandan, R. Yao, R. Sadangi, et al., J. Thermal Spray Technol. 9 (3) (2000) 329–331.
[9] H.L. de Villiers Lovelock, J. Thermal Spray Technol. 7 (3) (1998) 357–373.
[10] S.F. Wayne, S. Sampath, J. Thermal Spray Technol. 1 (4) (1992) 307–315.
[11] Y. Naerheim, C. Coddet, P. Droit, Surf. Eng. 11 (1) (1995) 11–15.
[12] T.P. Slavin, T. Nerz, in: T.F. Bernecki (Ed.), Thermal Spray Research and Applications, ASM International, 1991, pp. 159–164.
[13] C.J. Li, A. Ohmori, Y. Harada, J. Thermal Spray Technol. 5 (1) (1996) 69–73.
[14] Y.R. Liu, Y.F. Qiao, J.H. He, T.E. Fischer, E. Lavernia, Met. Mater. Trans. Part A 33 (2002) 159–164.
[15] G.R. Anstis, P. Chantikul, B.R. Lawn, D.B. Marshall, J. Am. Ceramic Soc. 64 (1981) 533.
[16] C. Verdon, A. Karimi, J.-L. Martin, Mater. Sci. Eng. A 246 (1998) 11–24.
[17] D.A. Stewart, P.H. Shipway, D.G. McCartney, Acta Mater. 48 (2000) 1593–1604.